Vacuum 201 (2022) 111092

Contents lists available at ScienceDirect

Vacuum

journal homepage: www.elsevier.com/locate/vacuum

Two-dimensional tungsten disulfide nanosheets and their application in self-powered photodetectors with ultra-high sensitivity and stability

Wilber Ortiz [a,*], Carlos Malca [a], Danilo Barrionuevo [b], Ali Aldalbahi [c], Elluz Pacheco [a], Nischal Oli [a], Peter Feng [a,**]

[a] Department of Physics, University of Puerto Rico, San Juan, 00931, USA
[b] Department of Mathematics and Physics, University of Puerto Rico, Cayey, PR, 00736, USA
[c] Department of Chemistry, College of Science, King Saud University, Riyadh, 11451, Saudi Arabia

ARTICLE INFO

Keywords:
2D tungsten disulfide nanosheets
Highly sensitive photodetector
High-throughput photocurrent
High optical absorption

ABSTRACT

Two-dimensional (2D) tungsten disulfide nanosheets (WS_2) could be a promising candidate for high-performance self-powered photodetectors. The present 2D nanosheets were obtained from liquid exfoliation in a mixture of ethanol, methanol, and isopropanol via a direct dispersion and ultrasonication method. Using the spin-coating technique, a thin film of uniform thickness was formed on the SiO_2/Si substrate. Energy-dispersive X-ray analysis showed that the S/W ratio in the fabricated WS_2 film was around 1.2 to 1.34, indicating certain deficiencies in the S atoms. These S vacancies induce localized states within the bandgap of pristine WS_2, resulting in a higher conductivity in the exfoliated sample. The obtained thin film seems to be highly efficient in photoelectric conversion, with a responsivity of ~0.12 mA/W at 670 nm under zero bias voltage, with an intensity of 5.2 mW/cm^2. Instead, at a bias of 2 V, it exhibits a responsivity of 12.74 mA/W and a detectivity of 1.17×10^{10} cm Hz$^{1/2}$ W^{-1} at 4.1 mW/cm^2. The present 2D nanosheets exhibit high photon absorption in a wide range of spectra from the near-infrared (IR) to near UV spectrum.

1. Introduction

2D transition metal dichalcogenides (TMDs) have excellent optical and electronic properties in creating sensitive photodetectors in the ultraviolet, visible, and infrared regions [1–5]. These materials exhibit immense potential in a wide range of applications due to their semiconducting properties, large absorption coefficient, sensitivity to interlayer interactions, and tunable bandgaps ranging from 1.4 to 2.1 eV according to the layer structure [6,7]. 2D tungsten disulfide nanosheets could be a promising candidate in new generation solar cells [8,9], gas sensors [10,11], photoluminescence [12,13], collision detectors, biomedical imaging, humidity sensor [14], optically filtered detectors [15], etc. Additionally, they present particularly interesting structures, owing to their high charge carrier mobility, high switching speed, and optical properties. Y.H. Tsang et al. [16] confirmed that WS_2 thin sheets contributed to a remarkably enhanced nonlinear optical absorption performance at 532 nm and 1064 nm.

In the fabrication of the 2D nanostructures, several methods have been used to obtain the WS_2 thin films on SiO_2/Si substrates. The most common TMDs were synthesized by chemical vapor deposition (CVD) [17], Magnetron Sputtering [18], Pulsed-Laser Deposition (PLD) [19], and sulfurization of metal films [20,21]. However, the liquid exfoliation method seems to be the most effective, particularly for quickly obtaining nanomaterials for light sensing applications, where a large quantity of 2D nanosheets with inherent defects are favorable for high carrier mobility. M. Terrones et al. [22] showed that chemical exfoliation methods have a scalability advantage over CVD. The challenge is to achieve the intercalation of bulk layered materials followed by efficient exfoliation without damaging the sheets. T.D. Anthopoulos et al. [23] informed that liquid-phase exfoliation of WS_2 yielded high concentration suspensions, where the extracted 2D nanosheets exhibited high structural and stoichiometric quality. This behavior is related to structural defects and strongly influences their optical properties. The deposition of the WS_2 liquid exfoliation by spin coating showed a decrease in the S/W ratio, indicating that the WS_2 film was deficient in S. These S vacancies induce localized states within the bandgap of pristine

* Corresponding author.
** Corresponding author.
E-mail addresses: wilber.ortiz1@upr.edu (W. Ortiz), peter.feng@upr.edu (P. Feng).

https://doi.org/10.1016/j.vacuum.2022.111092
Received 14 January 2022; Received in revised form 5 April 2022; Accepted 7 April 2022
Available online 12 April 2022

WS_2, generating a higher conductivity due to the S atoms induced defect states. For example, we showed a self-powered photodetector based on Au/WS_2/Au junctions, in which the responsivity reached 0.12 mA/W at 640 nm light illumination with 5.2 mW/cm^2 at a bias of 0 V. Instead, the R_λ was 12.74 mA/W at 640 nm with an intensity of 4.1 mW/cm^2 and at a bias of 2 V, respectively. Y.J. Yoon et al. [24,25] developed the direct WS_2 photodetector fabrication on a flexible substrate; the WS_2 film was less deficient in S, with an S/W ratio of 1.83, while the most deficient was 1.76. R_λ value was 0.53 mA/W at 635 nm with an intensity of 10.7 mW/cm^2 at a bias voltage of 10 V. Thus. S/W ratios are higher than our bulk material and even higher than exfoliated nanosheets, which also explains the need to apply a high bias. K. Huang et al. [26] also obtained an R_λ of 4.04 mA/W at 532 nm with an intensity of 59.09 mW/cm^2 at a bias of 5 V for a flexible broadband photodetector based on WS_2 nanosheets. Consequently, the device exhibits a lower electrical output per photon input than our prototype over the entire visible spectrum.

Since the device presented an excellent photoresponse to the mere action of light without the addition of an external power supply. It was found that the WS_2 film could activate the broader optical spectrum than the visible range, which makes it more attractive for applications of solar cells and broadband photodetectors (PDs). Xu et al. [27] studied oxygen-incorporated and layer-by-layer stacked WS_2 nanosheets for broadband and found that the photodetector is still sensitive at a wavelength in the NIR region (1100–2000 nm). These discoveries suggest great potential for future applications. Z. Wang et al. [28] also investigated flexible self-powered photoelectrochemical-type photodetector based on 2D WS_2-graphene heterojunction, recording a photocurrent density of 1.4 μA/cm^2 at an illumination intensity of 30 mW/cm^2. Thus, promoting the rapid migration of carriers and enhancing the optical response of TMDs.

In the present work, an exfoliation technique has been adopted via sonication in a mixture of ethanol, methanol, and isopropanol. The low boiling point of these solvents allows exfoliated nanosheets to have no extra steps required to remove these solvents since these are not pristine. Bulk TMDs crystals which have been exfoliated in solvents such as polymer solutions, *N*-Methyl-2- pyrrolidone (NMP), dimethylformamide (DMF), or surfactant solutions, are usually difficult to be removed from the surface of exfoliated nanosheets. The sample deposited on SiO_2/Si by the spin-coating method was characterized as a photoactive semiconductor that exhibits highly efficient photon absorption in a wide range of visible spectrums. Additionally, changes in voltage, temperature, and light intensities were made to observe the spectral response of a photodetector in the range of optical wavelengths to the influence of these physical magnitudes. The optimized sample improved the photocurrent's stability, especially in the near-infrared (IR) to the visible spectrum, making them suitable for solar cells and optoelectronic devices. The detailed results and sensing mechanisms are presented in this manuscript.

2. Experimental

2.1. Synthesis

WS_2 nanopowder (99% trace metal basis) and 90 nm avg part size was synthesized at a concentration of 1 mg/ml in a mixture of ethanol, 90%, methanol 5%, and isopropanol 5%. 1.5 g of WS_2 was dispersed in a 500 ml pyrex beaker with a magnetic stir bar placed within a solution volume of 250 ml. A digital stir plate drives the stir bar's motion beneath the vessel containing the solution for 2 h at 450 rpm. Then it was sonicated in a 500 W ultrasonic processor at 60 Hz amplitude with pulse On and Off times of 10 s for 10 h until a complete suspension of the powder in the solvent was achieved. Centrifugation at 3500 rpm for 30 min separated the suspended nanosheets from partially exfoliated WS_2. After standing for a few days in the Falcon beaker of 50 ml, three-fifths of the supernatants were collected using a 5 ml pipette.

We chose 5 × 1 mm^2 SiO_2/Si substrates to assess the optimum conditions of the WS_2 nanosheets. Both acetone, isopropanol, and deionized water were used to clean the substrate surfaces; then, it was dried at 100 °C for 15 min using a hot plate. The spin coating method was used to produce thin films with uniform thickness ranging. The exfoliated liquid was loaded onto the center of the substrate and spun for 15 s at 1200 rpm until the coating material spread on the whole surface edge. This sample was dried at 200 °C on a hot plate for 2 min to remove the solvent from the solution and monitor film growth. This procedure was repeated until a uniform surface of the WS_2 nanosheets was achieved, leaving a thin film of coating on the substrate.

2.2. Set-up

One back-to-back Schottky barrier structure was fabricated in the present study for a photodetector with Au/WS_2/Au junctions, as shown in Fig. 1. According to the synthesis method, WS_2 nanosheets based on liquid exfoliation were deposited onto the SiO_2/Si substrates. Then, the gold electrode elements were deposited in a vacuum chamber under an argon gas environment at a pressure of 5–8 mTorr by a sputtering technique at a power level of 250 W, where the aluminum foil was used as a mask to protect the middle portion of the thin film. The sputtering for 1 min yielded around 6 nm gold film on a 52 nm thick, 5 mm wide, and 1 mm long WS_2 film. The back-to-back Schottky diode was connected in series with an external resistor R_0 of 38 kΩ; then to an external power supply with adjustable voltage (V) from 0 to 2 V. Additionally, a heater was used to control the operating temperature of the photodetector device from 18 to 90 °C.

3. Results and discussion

3.1. WS_2 structure characterizations

Tungsten disulfide is an inorganic chemical compound with a layer structure of tungsten and sulfur atoms with the chemical formula WS_2, which occurs naturally as the rare mineral called tungstenite. This compound is part of the family of materials called the transition metal dichalcogenides. WS_2 has a two-dimensional structure with tungsten atoms positioned between two layers of sulfur atoms appearing in a trigonal prismatic coordination sphere-forming hexagonal crystals, as shown in Fig. 2a. Similarly, the single-layer or sheet projection of WS_2 (monolayer) onto the plane exhibits hexagonal structures (Fig. 2b), where atoms within each layer are connected through an ionic bond with a contribution of covalent interaction. In contrast, the multiple planes formed by the stacks are held together by weak van der Waals interactions.

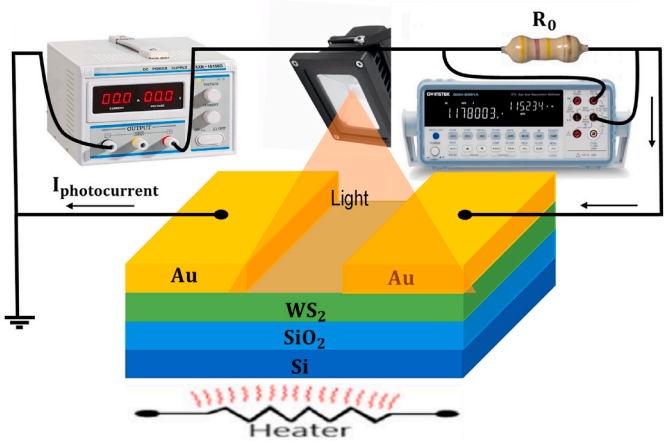

Fig. 1. Schematic representation of the photocurrent measurements set-up in Au/WS_2/Au contacts. Au is a solid conductor, while the WS_2 nanosheets are two-dimensional crystalline forms.

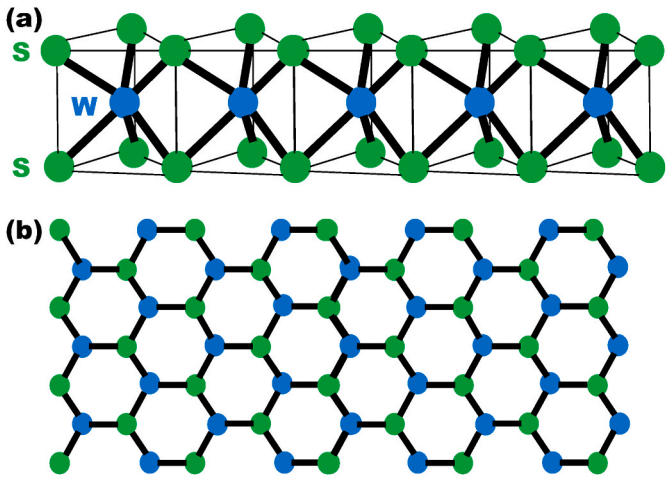

Fig. 2. Crystal structure of WS_2 with (a) tungsten atoms positioned between two layers of sulfur atoms and (b) single-layer projection of WS_2 onto the plane.

SEM image indicated that bulk WS_2 precursor consists of several thick hexagonal sheets with different diameters ranging from 100 nm to submicrometer and thickness of ~90 nm, as shown in Fig. 3a. After ultrasonic exfoliating, a large amount of flexible 2D nanosheets is clearly visible as shown in Fig. 3b, which is characteristic of multilayer thin films. In particular, the asymmetric growth of the nanosheets could be due to the weak interlayer coupling and the non-uniform size of the bulk sample. In addition, the horizontal and vertical orientation in certain substrate regions (SiO_2/Si) is partly attributed to the compression and extrusion between nanosheets. The obtained average width of the nanosheets was also reported to be in the range of 100–200 nm, while the thickness was in the order ~5 nm, which is similar to the morphology reported by X. Zhang et al. [29]. The spacing between the lattice fringes was approximately 0.64 nm, corresponding to two adjacent (002) basal planes of WS_2. These values can range from 0.62 to 0.65 nm according to the number of stacking layers in the mechanical exfoliation.

EDX analysis of bulk WS_2 precursor showed spatial distribution of elements through mapping, where the peak positions of each atomic structure were found in both the bulk material and the WS2 thin film. The most intense sharp peaks of W and S have the atomic percentage of 23.38 and 39.88, which gives an S/W ratio of 1.70, characteristics of the accurate composition of the bulk sample, as shown in Fig. 4a. After exfoliation, the atomic percentages of the elements in the WS_2 film were 1.85 and 2.49, respectively, and the S/W ratio was 1.34, which showed S atom deficiencies (Fig. 4b). We can verify that the S vacancies start in the mechanical exfoliation since the bulk material exhibits a higher S/W ratio than the dispersed nanosheets on the SiO_2/Si substrate. The weak van der Waals interactions between WS_2 individual layers allow easy exfoliation of the bulk structure, affecting some ionic-covalent bonds at the edges of the WS_2 monolayer that generate structural defects, mainly S vacancies, which in turn are substituted by oxygen atoms so as not to create defect states in space or an optically accessible subgap state in the WS_2 crystal structure. Byeong-Kyu Lee et al. [30] also showed that S atoms substituted for oxygen atoms during the oxidation process did not change the morphology structure of WS_2, but only the concentrations of the elements, which is consistent with the EDX results. But the chemisorbed oxygen can act as an electron receptor that alters the local intrinsic charge density, leading to recombination and optical properties changes. Previous studies by E. Stratakis et al. [31] demonstrated that chemisorbed oxygen, as well as physisorbed molecules (mainly O_2), affected the emission properties of exfoliated WS_2 single layers when sulfur was replaced by oxygen at the edges. These statements effectively support our analysis method on the mechanical exfoliation evolution of the bulk sample to the 2D WS_2 nanosheets.

S. Salehi and A. Saffarzadeh [32] studied that sulfur vacancies on the electronic structure of the monolayer induce a midgap band in the vicinity of the VBM, manifesting itself as defect states, which shift the Fermi level to the bottom of the conduction band due to unsaturated electrons in the Mo and W orbitals around the vacancy defect. This property suggests that the defect states induced by S vacancies in transition metal dichalcogenides can activate higher carrier mobility in the 2D WS_2 nanosheets and improve the photodetector's responsivity. A.K. Sharma et al. [33] observed a huge S deficiency in all WS_2 films deposited using the PLD technique. Where WS_2 film showed interesting linear and nonlinear optical properties, these arguments consolidate our assertions about the optical properties of S-deficient 2D WS_2 nanosheets.

On the other hand, EDX analysis of the atomic % of oxygen showed a relative increase from 2.07 to 5.05% after the exfoliation process. Since WS_2 has a two-dimensional structure with tungsten atoms positioned between two layers of sulfur atoms, the atomic % of W (1.85%) is expected to be less than S (2.49%). If the sample is pure, the ratio of S and W must be 2 to 1, which is impossible under ambient conditions and even in vacuum environments due to the interstitial defects of the lattice in the film growth process. In addition, the atomic % of carbon in the bulk sample and the thin film was reported to be much higher than rest of the elements, this usually happens when a thin layer of carbonaceous material is found on the air-exposed samples, which is generally known as adventitious carbon.

The nanosheets' X-ray diffraction (XRD) patterns were compared with the commercial WS_2 nanopowder, as shown in Fig. 4c. The bulk WS_2 and the exfoliated products have a highly crystalline structure with the most intense and sharp peak at $2\theta = 14.15°$, corresponding to the (002) crystallographic plane consistent with the hexagonal phase WS_2 (2H-WS_2), as shown in Fig. 2a. However, nanosheets do not exhibit other peaks as in the bulk material ((004), (100), (103), (106), (105), (110), and (112)); there is only the addition of the silicon peak due to the contact between the substrate and the sample, as shown in Fig. 4d. These absences confirm that the nanosheets were exfoliated along the (002)

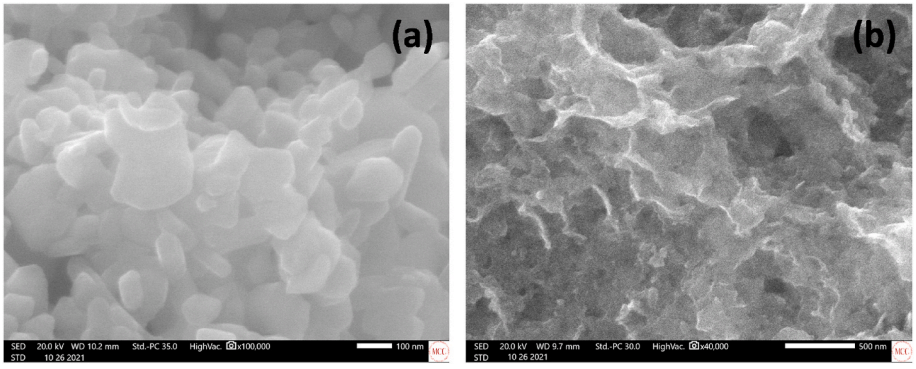

Fig. 3. Scanning electron microscopy (SEM) images of the (a) bulk WS_2 precursor and (b) two-dimensional (2D) nanosheets.

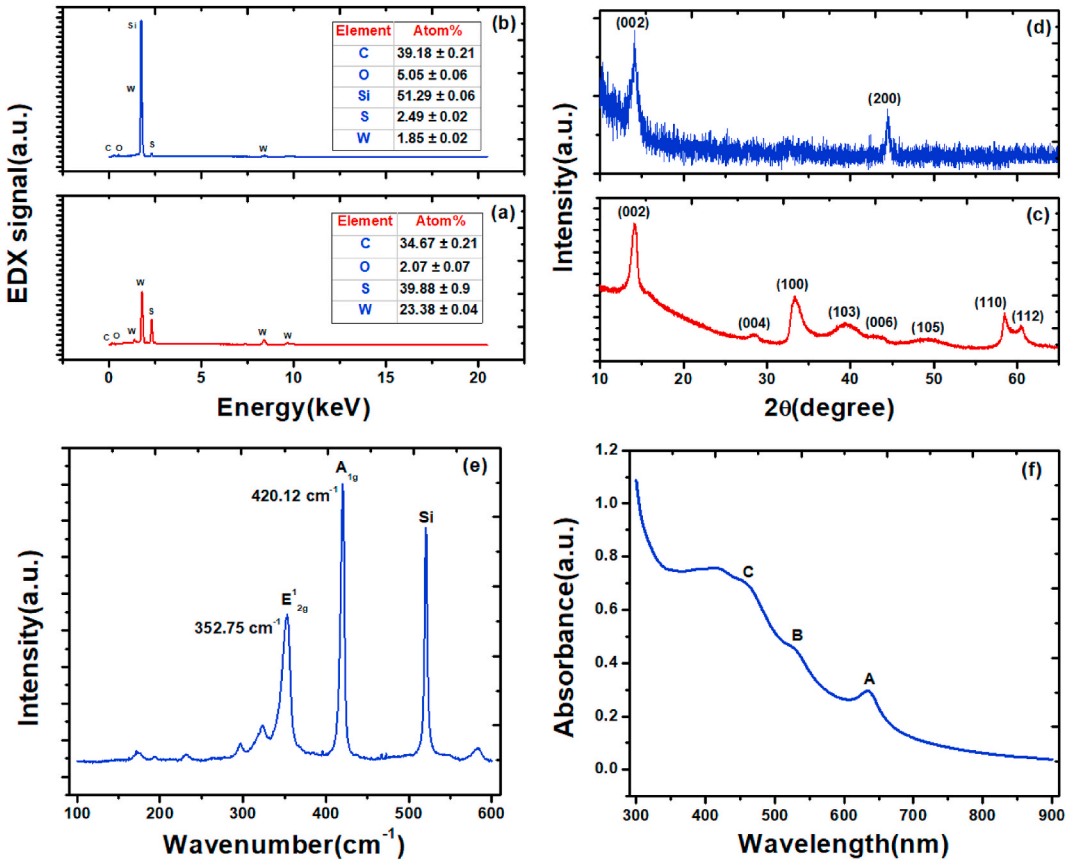

Fig. 4. EDX analyses of (a) bulk WS_2 precursor and (b) after exfoliation, (c) X-ray diffraction (XRD) patterns of the bulk precursor, and (d) after exfoliation, (e) Raman scattering spectrum, and (f) UV–visible absorption spectra of the WS_2 nanosheets.

plane, leading to the enhanced intensity in XRD measurement preferentially orientated into substrates with the (002) basal plane parallel to the substrate. Compared with the intensity of bulk WS_2, those of the nanosheets was reduced by more than half. This is a consequence of the effective lateral size reduction and the high degree of delamination of the bulk sample in the exfoliation process. The obtained diffraction peaks indicated that the surface of the nanosheets did not show other impurities that could significantly affect the crystallinity and original structure of the sample. Another detail of the XRD pattern is the disappearance of peaks 33.34° and 58.52°, corresponding to the (100) and (110) planes. This proves that the number of stacked layers decreases significantly compared to the bulk WS_2, i.e., exfoliation-assisted nanosheets consist of few layers, which reduces energy states. Using Bragg's law, we calculated the interlayer distance at WS_2 film through relation $d = \frac{n\lambda}{2\sin\theta}$, where λ is the wavelength of the x-ray source (λ = 1.54 Å), n is the order of reflection ($n = 1$), and θ is the angle of incidence in degrees of the plane (002). The interlayer spacing of 2D WS_2 nanosheets turns out to be ~0.64 nm, respectively. This value suggests that the stacked nanosheets are sturdily coupled due to the strong van der Waals interactions.

The Raman spectrum of the WS_2 nanosheets shows two peaks at 352.75 and 420.12 cm^{-1} belonging to the Raman active vibrational modes, assigned to E^1_{2g} and A_{1g} phonon modes 2H-WS_2, respectively. The peak corresponding to E^1_{2g} involves two-mode behavior, i.e., the in-plane displacement of W and S atoms. In contrast, for A_{1g} vibration, only S atoms vibrate, indicating one-mode behavior. However, A_{1g} mode always has a stronger peak than that E^1_{2g} mode when the laser light incident about WS_2 nanosheets thin films in the Raman scattering method, as shown in Fig. 4e. A_{1g} has been used as a mechanism to trace the signature of mono, and a few layers in the TMD samples since the vibrational spectrum is sensitive to the number of layers. For example, as the WS_2 layer thickness increases, the A_{1g} mode intensity increases due to the increase in S atoms. Since it rests on the separation between the short-range interatomic force constants, the weak interlayer interactions are dominant. Thus, the exchange of S atoms with the nearest layers is crucial in A_{1g}-mode changes to the interlayer coupling. Meanwhile, E^1_{2g} is attributed to the long-range Coulomb interactions with macroscopic electric fields acting in the shift in frequency between longitudinal optical (LO) and transverse optical phonons (TO) about the neighborhood of the Brillouin zone center. The origin of this LO-TO splitting can be understood most readily if one considers an argument of P. Giannozzi et al. [34].

The UV–visible absorption spectra of the WS_2 nanosheets exhibit a prominent peak at 634 nm and a small peak at 528 nm corresponding to the characteristic excitonic A band and indirect B excitonic transition, as shown in Fig. 4f. In contrast, the C band at 456 nm is not fully resolved. Due to optical transitions between the density of states (DOS) peaks in the valence and conduction bands, it is treated as the transition from an indirect-to-direct bandgap. The origin of these transitions is attributed predominantly to the interlayer coupling effect or quantum confinement, which controls the bandgap evolution according to the spatial confinement of electron-hole pairs in one or more 2D WS_2 nanosheets. L. Zhang and A. Zunger [35] also suggested that the dominating physical factor on the layer thickness for all the MX_2 (M = Cr, Mo, W and X = S, Se, Te) was the quantum confinement effect, where the energy level of nanostructures increased as the result of increased kinetic energy when the size of nanostructures reduced. Electronic energy levels in this configuration are discrete, so the nanosheets' optical energy absorption is within allowed levels—these contras with the excitonic energy levels and the optical absorption of light in the visible range. Thus, the photoluminescence energy of excitons helps us understand the evolution of the electronic structure as a function of the number of layers.

Band structure of bulk WS_2 has an indirect bandgap in the range 1.3 eV < ΔEg < 1.4 eV, and it increases as the number of stacked layers decreases until reaching a value of 2.05 eV, corresponding to the total density of states for the WS_2 monolayer, which is the direct bandgap at the K point of Brillouin zone, respectively [36,37]. In bulk, transitions A and B observed by absorption spectroscopy are direct optical transitions at K point and calculated as excitons A (1.95 eV) and B (2.35 eV), using the equation $E_g = \frac{hc}{\lambda}$, where E_g is the energy gap, h is the Plank's constant (6.6267×10^{-34} J s), c is the speed of light (3.0×10^8 m/s), and λ is the wavelength of light. Thus, the UV–visible absorption spectrum data confirms the existence of a few-layer WS_2 film and is consistent with the previous analysis reported in the literature. The first peak at the long wavelength of 634 nm, corresponding to WS_2 nanosheets, has an optical bandgap of 1.95 eV, higher than the bulk sample value of about 1.35 eV. An increase in bandgap is a clear indication of quantum confinement among the stacked few-layered. In addition, 1.95 eV < 2.05 eV, confirming that the binding energy of the monolayer WS_2 is higher than that of nanosheets. Therefore, exciton transition A allows us to identify the quality of the exfoliation and the optical absorption of the sample.

3.2. Schematic bandgap alignment diagram in the carrier transport

Fig. 5 shows the schematic energy band alignment diagrams for the particular case of two back-to-back Schottky diodes in Au/WS_2/Au contacts. Under dark conditions and without applying a bias voltage, the device exhibits a symmetric Schottky structure under the same vacuum level, as shown in Fig. 5a. Alignment of Fermi energy leads to the formation of band diagrams in the metal/semiconductor interface states, where Φ_B is the barrier height, E_F is the Fermi level of the semiconductor, E_v is the valence band edge, E_c is the conduction band edge, V_i is the built-in-voltage barrier, and W_0 is the thickness of the depletion region, which depends on the concentration of ionized acceptor atoms. Since each Schottky barrier acts as a current rectifier, electrons can move from the semiconductor to metal and be controlled by two sides of the interface in equilibrium (constant barrier height) if there is no external effect on the system. However, electron-hole pairs are generated when an amount of voltage is supplied, creating the charge flow and voltage drops on single diodes, as shown in Fig. 5b. Electrons tend to move toward a positive bias because the voltage drop from V_2 ($V_2 < V_i$) induces a narrow depletion region (W_2) than V_1 ($V_1 > V_i$) with W_1, which changes the Schottky barrier height, as well as the direction and magnitude of the dark current. In addition, not all valence electron becomes free electrons, so lattice defects trap some in the two-dimensional layers of the semiconductor. The increased external power supply will lower the barriers and extract more charge carriers from the trap states, thus increasing the net dark current due to a larger electric field.

Under illumination and zero bias voltage, the barrier heights depend on the generation and recombination of photogenerated charge carriers when the photodetector device absorbs the light. The excitation of an electron or other charge carrier to a higher-energy state produces an electrical potential by the separation of charges by diffusion. Therefore, depending on the concentration of carriers in the metal-semiconductor junction, the photocurrent can take any direction, as shown in Fig. 5c.

Under bias voltage and illumination, photogenerated charge carriers start distribution at metal/semiconductor interfaces. Depending on the charge accumulation process, the Schottky barrier height of the two interfaces tends to vary further due to bandgap light excitation and the addition of voltage, which allows the magnitude of the electric field to increase further, as shown in Fig. 5d. Thus, additional photogenerated charge carriers are swept from the trap states of the photodetector and move by hopping process from the semiconductor to the barrier interfaces, thus generating a reduction in the resistance of the device and an increase in the photocurrent due to the tunneling of carriers.

3.3. Photovoltaic mode operation

Succeeding characterizations, the photoelectric current was studied in a photosensitive device designed as a back-to-back Schottky diode under the light on/off mode, as shown in Fig. 6a. In this test, no external power supply was used. Only 670 nm light-induced photocurrents (I_{ph}) at the illumination intensity ($I_{intensity}$) of 5.2 mW/cm^2 on the surface of the active layer was measured. When the illumination was applied, the light-induced photocurrent immediately generated up to 3.06×10^{-8} A, and when the light was turned off, it was instantly restored to zero. Such a photovoltaic effect was reproduced during multiple testing cycles in 20 s. These results indicate that the developed photosensitive semiconductor device shows an excellent photoresponse to illumination in the near-infrared region of the electromagnetic spectrum. Similarly, at ranges of light wavelengths from 420 to 605 nm, the photodetector device responded selectively and stably, revealing a strong photoresponse at 670 nm, as shown in Fig. 6b and c. Alternation of the

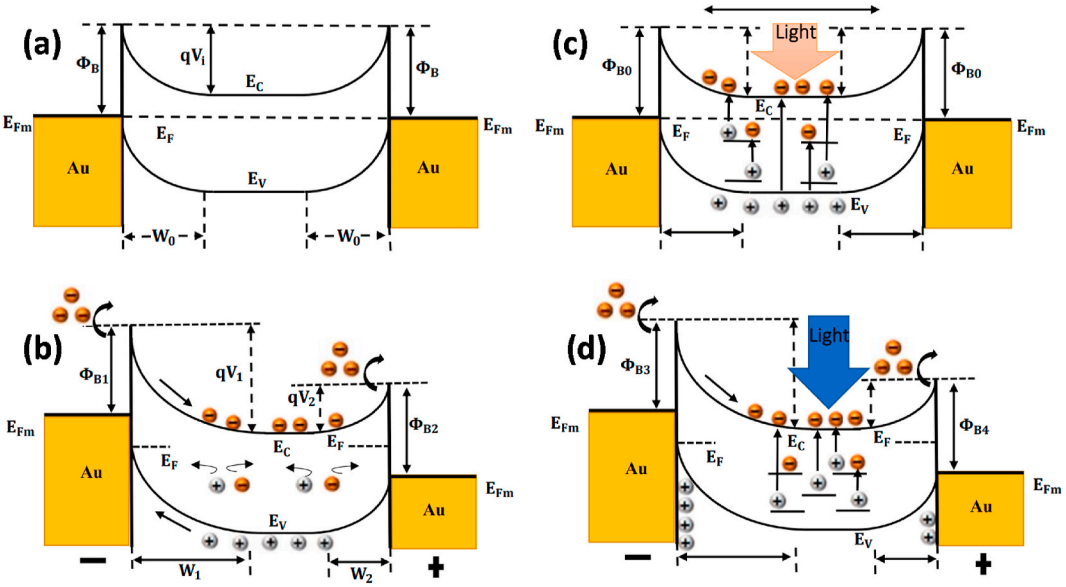

Fig. 5. Schematic energy band alignment diagrams. Under dark conditions (a) without and (b) with bias voltage. Under illumination (c) without and (d) with bias voltage.

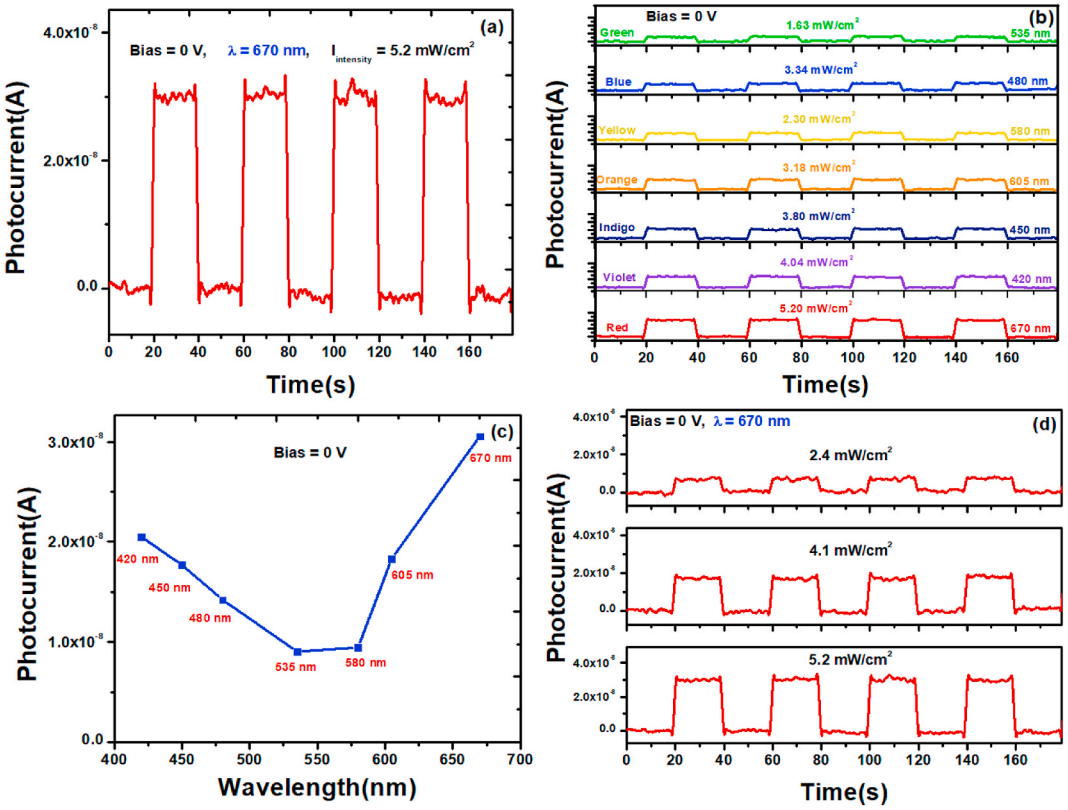

Fig. 6. Photodetector device designed as back-back Schottky diode (Au/WS_2/Au). (a) Photocurrent-time cyclical curve under cyclical illumination at 5.20 mW/cm^2, (b) photocurrent-time curves at light intensities from 1.63 to 5.20 mW/cm^2, (c) photocurrent-wavelength curve, and (d) photocurrent-time curves excited with 670 nm light at different illumination intensities.

excitation source between the green and red light for the integrated photodiode results in switching of photocurrents between 2.45×10^{-8} A and 3.1×10^{-8} A, respectively, the latter being because of higher photon absorption in the near-infrared than the rest of the spectra. Photocurrent transport properties in the photovoltaic semiconductor are dependent on light excitation frequencies. This behavior is closely related to the photoelectric effect, as well as to physical and chemical phenomena. In both cases, the light spectrum absorbed by the 2D WS_2 nanosheets is dominated by discrete energy states that condition the charge carrier excitation to a higher energy level that is still contained within the sample. This effect generates a photovoltage by separating charges by diffusion, and the illumination pattern must have sufficient energy to overcome the potential barrier for excitation. If we look at Fig. 6b and c, we can see that each colour of light has a different wavelength and, therefore, excitation energy change defines the generation of charge carriers in the Au/WS_2 contact.

The behavior of the 2D WS_2 nanosheets as a multilayer structure seems to have high efficiency in absorbing photons in a wide range of frequencies to the mere action of light. The top layer nanosheets absorb shorter wavelengths, and the bottom converts the longer ones, as UV–visible absorption spectrum data confirms, giving significantly better conversion efficiency and better photocurrent output. Newer photovoltaic cell designs achieve higher efficiency by converting more lights into useful electrons, so expectations are promising for future applications. In addition, 2D WS_2 nanosheets with deficient S atoms could minimize the energy barrier and charge accumulation at the interface to enhance the extraction of photoinduced charge separations and carrier-transfer dynamics in photovoltaic devices.

To further study the effect on the performance of the photodetector device, we define the photocurrent as:

$$I_{ph} = I_{light} - I_{dark} \tag{1}$$

$$I_{ph} = c\left(I_{intensity}\right)^{\alpha} \tag{2}$$

where I_{light} is the photocurrent under illumination, I_{dark} is the dark current or the unwanted leakage current, c is a proportionality constant of 6×10^{-10}. α is an empirical value of 0.93 between 0.5 and 1, indicating that the saturation is mainly due to the photogenerated carriers' kinetics involving recombination states and carrier-carrier interactions. This behavior plays a vital role in determining the performance of fast optoelectronic devices.

The illuminating of the light source (P) and the responsivity of an ideal photodetector (R_λ) are described by equations:

$$P = I_{intensity} \times A \tag{3}$$

$$R_\lambda = \frac{I_{ph}}{P} \tag{4}$$

where A is the active layer surface of the WS_2 film (5×10^{-6} m^2). The responsivity of the device with a bias voltage of zero reached values from 0.1 to 0.12 mA/W in almost the full spectrum of visible light under intensities from 1.2 to 4.1 mW/cm^2. Previous studies by Y.J. Yoon et al. [25] showed the R_λ value in large-area and low-temperature synthesis of few-layered WS_2 films for photodetectors, fabricating by sputtering with 3 kV EBI was 0.19 mA/W at wavelength of 635 nm with intensity of 10.7 mW/cm^2 at a bias voltage of 10 V. Similarly, Y.J. Yoon et al. [24] developed the direct WS_2 photodetector fabrication on a flexible substrate using 1 kV EBI treatment, where R_λ value was 0.53 mA/W, respectively. These measures are not significantly large compared to the R_λ of our material, characterized under zero bias. This may be because the light S atoms are not so deficient in WS_2 thin-film growth since the S vacancies generate most carrier generation and carrier recombination. According to Yoon, the WS_2 film was less deficient in S, with a S/W ratio

of 1.83, while the most deficient was 1.76. These values are higher than our bulk material (S/W = 1.70) and even higher than exfoliated nanosheets (S/W = 1.3), which also explains the need to apply a high bias in photodetectors fabricated with kV EBI treatment. M. Terrones et al. [38] also characterized photosensor devices based on few-layered WS_2 films, where the smallest spectral photoresponse was 2.0 μA/W, a value measured for the red laser of 647 nm, while the highest recorded photoresponse corresponded to 21.2 μA/W, measured with the blue laser of 458 nm at a bias of 5 V. The optical signal magnitudes of our prototype are much higher than the photosensors of Terrones fabricated using the CVD technique. Although the article did not report the atomic concentrations of S and W, we believe that the absence of S vacancies could be the answer to the low signal at a high bias. An additional advantage of the works of Ali Aldalbahi et al. [39] in the mechanical exfoliation of two-dimensional atomic layer molybdenum disulfide showed high responsivity at wavelengths of 670 nm, where photocurrent measurements were also comparable to the values of 2D WS_2 nanosheets. Therefore, S deficiency and layer stacking of the bulk sample seem to induce higher mobility of charge carriers at low light intensity.

Given that R_λ is used to evaluate the sensitivity of a photodetector, we can say that our material generates a higher photocurrent at low illumination of the light source. This is attributed to the fact that the setting curve follows a power law of photocurrent and light intensity, resulting in more photocurrent generated through the metal-semiconductor junction with a low trapping effect in the width of the depletion region is broadened. Captured carriers are reduced with increasing light power intensity; conducting, more photogenerated electron-hole pairs can contribute to the photocurrent.

Table 1 shows the performance of some WS_2-based photodetectors on different substrates, fabrication methods, and illumination intensities in the visible spectrum.

When the distance between the light source and the WS_2 thin film was varied, the light intensity on the surface of the active layer decreased as the distance increased, as shown in Fig. 6d. The 670 nm light-generated photocurrent was 3.1×10^{-8} A at 5.2 mW/cm^2, 1.8×10^{-8} A at 4.1 mW/cm^2, and finally 0.82×10^{-8} A at 2.4 mW/cm^2, respectively. The photocurrent value decreases as the light power density decreases. This mechanism is because there is an inverse relationship between distance squared and light intensity, i.e., as the distance away from a light source increase, photons of light become spread over a wide area before reaching the WS_2 thin film. The responsivity of the device also decreases slightly, as it is directly proportional to the photocurrent or power law of intensity. However, the periodic On/Off cycles of 20 s showed excellent stability under environmental conditions, except for the photocurrent changes due to the decrease in light intensity.

Temperature-correlated photocurrent measurement was performed to validate its viability under normal operating conditions of the photodetector, where the 2D WS_2 nanosheets showed higher sensitivity to light in a wide range of wavelengths. The results verify the effectiveness and stability of the device up to an acceptable temperature range, as shown in Fig. 7a and b. As the temperature goes up, the absorption depth of light decreases slightly, which could be due to a significant amount of carriers being recombined because of the non-uniform concentration of WS_2 atoms by the vacancies of S. Therefore, changes in environment temperature affect the device more in photovoltaic mode than in photoconductive mode of operation (reverse biasing). According to the back-to-back Schottky diode's biasing conditions, the anode and cathode are at the same potential in a photovoltaic implementation, i.e., the diode is zero-biased. This implies that the device depends on the generation and recombination of photogenerated charge carriers, the wavelength of the incident light, and the Schottky barrier heights. In addition to this is the temperature dependence of the bandgap, which varies according to the number of stacked layers of the 2D WS_2 nanosheets. For example, the liquid exfoliation of the bulk WS_2 sample showed a direct optical transition of 1.95 eV, which was lower than that of the monolayer (2.05 eV). This allows us to infer that nanosheets with a reduced number of layers may be more resistant to degradation as temperature increases.

On the other hand, the weak Schottky barrier allows the prototype to act as an ohmic contact for a self-powered photodetector in the entire visible spectrum at intensities from 1.6 to 5.2 mW/cm^2, as shown in Fig. 7c. Electrical current can be conducted in both directions of the M − S contact when the WS_2 nanosheets absorb the photons of light to generate pairs of electrons and holes; such the electron diffuses from the metal to the semiconductor, thus increasing the concentration of electrons and not causing depletion of the semiconductor near the junctions. Photodetectors with these features are required since external contacts to a photovoltaic cell need to be ohmic to prevent an unnecessary voltage drop at the contact. Therefore, the low contact resistance and a junction between M − S that has a linear photocurrent-photovoltage curve, as with Ohm's law, are critical for the performance and reliability of semiconductor devices.

The rise and decay times of the WS_2 based prototype exposed to 670 nm light illumination were also measured. The rise time (1.20 s) was slightly longer than the decay time (1.21 s) but with a difference of 0.01 s in the switching change. When the light source was On mode, the photocurrent quickly raised to a high-level steady state, followed by a relatively slow tail, while a reversed behavior was observed when the light switched off, as shown in Fig. 7d. This response speed is faster than

Table 1
Comparisons of the performances of WS_2-based photodetectors.

Year	Substrate	Fabrication Method	Wavelength [nm]	Intensity [mW/cm^2]	Responsivity [mA/W]	Detectivity [cm Hz W^{-1}]	Bias Voltage (V)
2021	Polyimide [24]	Sputtering with 1 kV EBI treatment	450	14.9	1.25	2.52×10^7	10
			532	3.9	1.66	3.34×10^7	
			635	10.7	0.53	1.08×10^7	
2018	SiO_2/Si [25]	Sputtering with 3 kV EBI treatment	450	14.9	0.36	–	10
			532	3.9	1.37		
			635	10.7	0.19		
2020	Flexible filter membrane [26]	Vacuum filtration	532	59.09	4.04	2.55×10^9	5
2018	SiO_2/Si [41]	CVD	532	450	5	–	10
2013	Quartz [38]	CVD	647	–	2×10^{-3}	–	5
			458		21.2×10^{-3}		
			514		0.21×10^{-3}		
Our work	SiO_2/Si	Spin coating	420	3.16	0.102	1.0×10^8	0
			450	2.95	0.100	0.9×10^8	
			670	4.13	0.120	1.35×10^8	
			420	3.16	12.0	1.10×10^{10}	2
			450	2.95	10.0	0.91×10^{10}	
			670	4.13	12.74	1.20×10^{10}	

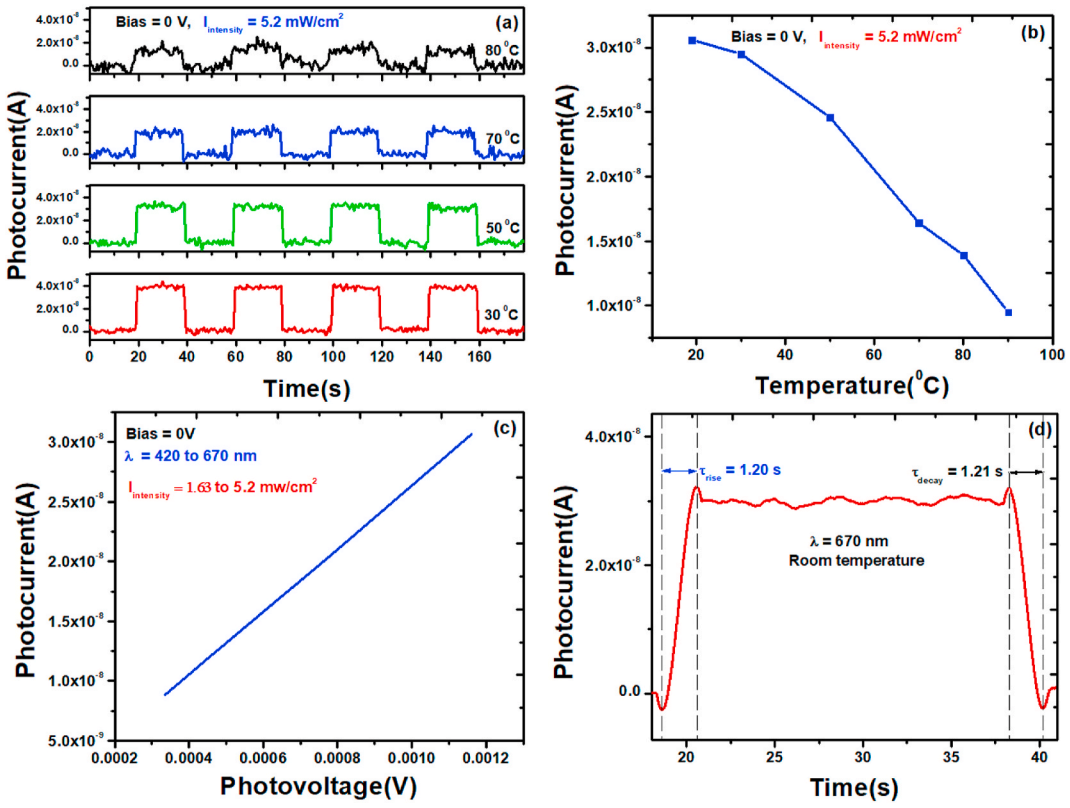

Fig. 7. (a, b) Temperature-correlated photocurrent curves under operating conditions from 19 to 90 °C at a light intensity of 5.2 mW/cm^2, (c) photocurrent-photovoltage curve at ranges of light wavelengths from 420 to 605 nm and intensities from 1.63 to 5.2 mW/cm^2, and (d) rise and decay times of Au/WS_2/Au photodetector device under the illumination of switched On/Off in periods of 20 s.

highly responsive and broadband photodetection based on large-area multilayered WS_2 films grown by pulsed-laser deposition, as reported by G. W. Yang [40]. In our case, we characterized at zero bias.

The detectivity (D*) evaluates the device's sensitivity to weak optical signals. The equation that describes this parameter is:

$$D^* = \frac{R_i A^{1/2}}{(2qI_{dark})^{1/2}} \quad (5)$$

where A is the area of the photosensitive region of the detector and I_{dark} is the dark current (1.84×10^{-7} A). When performing the calculation, a value of 1.35×10^8 cm Hz W^{-1} was obtained at 5.2 mW/cm^2, representing the acceptable value of a high-performance photodetector under zero bias. A device with these characteristics can be attributed to the higher mobility and absorption of present WS_2 nanosheets-based film, associated with increased carrier recombination dynamics and excellent photoresponse at low light intensities. Thus, confirming that the signal/noise ratio is within the allowed standards for a self-powered photodetector. However, as the temperature increases, the detectivity of the device decreases due to increased signal/noise.

3.4. Bias effect

Variation characteristics as a function of time have been explored for the photodetector device to a 670 nm light illumination at different applied biases and a light intensity of 4.1 mW/cm^2, as shown in Fig. 8a. Similar to the previous case, the illumination of switched on/off was set in periods of 20 s during several testing cycles. The device exhibited switching behavior and repeatability without degradation at bias voltage ranges from 0.5 to 2 V. The typical photocurrent response of the device to the light source increased from 2.0×10^{-7} to 2.6×10^{-6} A with an increase of bias. Thus, a high bias and light irradiation favor the fast separation and transportation of the photoinduced charge carriers to the working electrodes, increasing the photocurrent, as shown in Fig. 8b. As the width of the depletion region is broadened, the built-in electric field of the optical metal-semiconductor heterostructure is enhanced, generating recombination of photo-generated electron and hole pairs favor the rapid separation of the photogenerated charge carriers, resulting in the increment of photocurrent and a faster response time to the On/Of light cycles as the bias voltage increases. With the depletion layer (forward bias) reduction, charge traps generated by interstitial impurities, S vacancies, and lattice defects are minimized, which also contributes to a higher photocurrent between WS_2/Au junctions.

Performing cyclic tests under On/Off mode at a bias of 2.0 V, good repeatability and a stable baseline were visible when the device was exposed to 670, 420, and 450 nm at the same distance between the sample and the light source, respectively. When generating light-induced photocurrents, the prototype's conversion efficiency for red illumination appears to be higher than that for the violet and indigo spectra (Fig. 8c), reaching a responsivity of 12.74 mA/W to 670 nm, as shown in Fig. 8d. This value is more significant than that of the growth of wafer-scale standing layers of WS_2 for self-biased high-speed UV–visible–NIR optoelectronic devices grown by the CVD technique, where the responsivity and intensity were 450 mW/cm^2 and 5 mA/W at a bias voltage of 10 V, according to the measurements obtained by J.C. Ho et al. [41]. Similarly, K. Huang et al. [26] characterized a flexible broadband photodetector based on WS_2 nanosheets films obtained by the vacuum filtration method, reaching a spectral photoresponse of 4.04 mA/W at 532 nm with an intensity of 59.09 mW/cm^2 at bias of 5 V. These values exhibit a lower electrical output per photon input than our photodetector device. In addition, under 2 V detectivity reached up to 1.2×10^{10} cm Hz$^{1/2}$ W^{-1}, which confirms the intrinsic quality of the prototype. This photodetector device that exhibits highly sensitive to the light intensity are even better than WS_2 photodetectors shown in Table 1

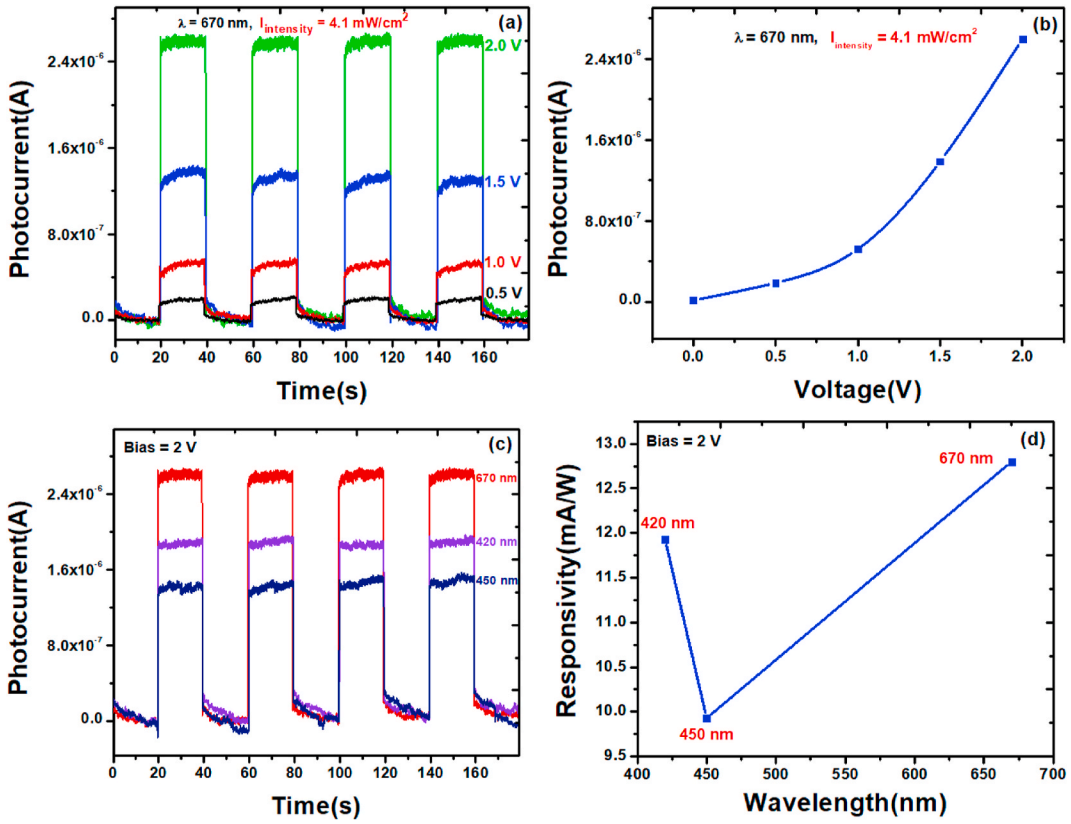

Fig. 8. The bias voltage effect on the fabricated photodetector was exposed to the light intensity of 4.1 mW/cm^2. (a) Photocurrent-time curve under On/Off mode with bias from 0.5 to 2 V on the spectral response of 670 nm, (b) photocurrent-voltage curve from 0 to 2 V, (c) photocurrent-time curve under On/Off mode on the spectral responses from 420 to 670 nm at 2 V, and (d) responsivity-wavelength curve at 2 V.

due to the rapid separation of photogenerated carrier at the Au/WS_2 interface.

Therefore, 2D WS_2 nanosheets exhibit a better absorption for the light spectra of 420 nm and 670 nm, the latter being the maximum intensity in the visible range due to the higher number of optically generated carriers with an excitation photon energy of about 1.85 eV of the bandgap. This value is within the range of the direct optical transitions at the K point of Brillouin zone for exciton A. Accordingly, the quantum confinement in WS_2 nanosheets defines the absorption of light in the visible range. If adding a bias voltage of 2 V on the illuminated nanosheets terminals, the magnitude of the electric field increases, generating additional photogenerated charge carriers from the semiconductor to the barrier interfaces, which improves responsivity and detectivity.

4. Conclusions

2D nanosheets deficient in S showed a higher photon absorption in the near-infrared range with a photocurrent output of 3.06×10^{-8} A and a detectivity of 1.35×10^{8} cm Hz W^{-1} at 5.2 mW/cm^2, which is the acceptable value of a high-performance photodetector under zero bias. Similarly, the responsivity of the device reached a deal of ~0.12 mA/W, several orders of magnitude larger than photosensor devices based on few-layered WS_2 films grown by the CVD technique. These results suggest that the high degree of delamination of the bulk sample improves the light absorption in 2D WS_2 nanosheets in a wide range of the visible spectrum. In addition, the defect states induced by S vacancies in the quantum confinement process improve the mobility and photogenerated charge carriers. The direct optical transition of 1.95 eV, close to the band structure of monolayer transition, allows the exfoliated nanosheets along the (002) plane to be highly stable to light On/Off cycles, even be more resistant to degradation in higher temperature environments.

At 2 V, the responsivity was 12.74 mA/W and a photocurrent of 2.6 $\times 10^{-6}$ A at 4.1 mW/cm^2, which is better electrical output per light input than flexible broadband photodetectors based on WS_2 nanosheets films obtained by the vacuum filtration method. This value was also larger than that of the growth of wafer-scale standing layers of WS_2 for self-biased high-speed UV–visible–NIR optoelectronic devices grown by the CVD technique, where the responsivity and intensity were 450 mW/cm^2 and 5 mA/W at a bias voltage of 10 V. In addition, the detectivity of 1.2×10^{10} cm $Hz^{1/2}$ W^{-1} exhibited high sensitivity to the light intensity than WS_2 photodetectors fabricated by sputtering with EBI treatment and CVD technique, where the values ranged from 10^7 to 10^9 cm $Hz^{1/2}W^{-1}$ at bias voltages of 10 and 5 V, respectively. Thus, nanosheets exhibit high sensitivity and enhanced photoresponse when the built-in electric field of the optical Au/WS_2/Au heterostructure is increased. The rapid recombination and separation of the photogenerated carriers significantly reduce charge traps in the Au/WS_2 interface; similarly, the depletion layer becomes narrower and allows the barrier to carrier injection in the forward bias direction to be reduced. Illumination at 670 nm also provides a higher density of carriers from the bandgap to the conduction band, thus showing a higher optical signal than the rest of the visible spectrum.

Our studies also showed that WS_2 thin film with inherent defects and transparent sample improves light absorption over a wide range of the optical spectrum. Hence, on a transparent substrate, it is possible to obtain a better photoresponse of the device with appropriate control in the growth of the layers since almost all light passes directly through them. Unlike the most expensive instruments, the liquid exfoliation method of 2D materials offers a facile and low-cost technique to produce mono- and few-layer 2D nanosheets in a commercially viable way.

CRediT authorship contribution statement

Wilber Ortiz: Conceptualization, Data curation, Formal analysis, Funding acquisition, Investigation, Methodology, Writing – original draft, Writing – review & editing. **Carlos Malca:** Methodology. **Danilo Barrionuevo:** Conceptualization, Investigation, Methodology. **Ali Aldalbahi:** Conceptualization, Methodology, Validation. **Elluz Pacheco:** Methodology. **Nischal Oli:** Methodology, Resources. **Peter Feng:** Conceptualization, Formal analysis, Investigation, Methodology, Supervision, Writing – review & editing.

Declaration of competing interest

The authors declare that they have no known competing financial interests or personal relationships that could have appeared to influence the work reported in this paper.

Acknowledgments

This work is financially supported by NSF-CREST Center for Innovation, Research, and Education in Environmental Nanotechnology (CIRE2N) Grant Number HRD-1736093. The authors acknowledge the King Saud University, Riyadh, Saudi Arabia, for funding this work through Research Supporting (Project No. RSP-2021/30). University of Puerto Rico Molecular Science Research building (MSRB) offers specialized services with research equipment.

References

[1] W. Choi, N. Choudhary, G.H. Han, J. Park, D. Akinwande, Y.H. Lee, Recent development of two-dimensional transition metal dichalcogenides and their applications, Mater. Today 20 (2017) 116–130, https://doi.org/10.1016/J.MATTOD.2016.10.002.

[2] D. Wu, J. Guo, J. Du, C. Xia, L. Zeng, Y. Tian, Z. Shi, Y. Tian, X.J. Li, Y.H. Tsang, J. Jie, Highly polarization-sensitive, broadband, self-powered photodetector based on graphene/PdSe2/germanium heterojunction, ACS Nano 13 (2019) 9907–9917, https://doi.org/10.1021/ACSNANO.9B03994.

[3] L.H. Zeng, D. Wu, S.H. Lin, C. Xie, H.Y. Yuan, W. Lu, S.P. Lau, Y. Chai, L.B. Luo, Z. J. Li, Y.H. Tsang, Controlled synthesis of 2D palladium diselenide for sensitive photodetector applications, Adv. Funct. Mater. 29 (2019), 1806878, https://doi.org/10.1002/ADFM.201806878.

[4] D. Wu, J. Guo, C. Wang, X. Ren, Y. Chen, P. Lin, L. Zeng, Z. Shi, X.J. Li, C.X. Shan, J. Jie, Ultrabroadband and high-detectivity photodetector based on WS2/Ge heterojunction through defect engineering and interface passivation, ACS Nano 15 (2021) 10119–10129, https://doi.org/10.1021/ACSNANO.1C02007/SUPPL_FILE/NN1C02007_SI_001.PDF.

[5] L.H. Zeng, S.H. Lin, Z.J. Li, Z.X. Zhang, T.F. Zhang, C. Xie, C.H. Mak, Y. Chai, S. P. Lau, L.B. Luo, Y.H. Tsang, Fast, self-driven, air-stable, and broadband photodetector based on vertically aligned PtSe2/GaAs heterojunction, Adv. Funct. Mater. 28 (2018), 1705970, https://doi.org/10.1002/ADFM.201705970.

[6] H.L. Liu, C.C. Shen, S.H. Su, C.L. Hsu, M.Y. Li, L.J. Li, Optical properties of monolayer transition metal dichalcogenides probed by spectroscopic ellipsometry, Appl. Phys. Lett. 105 (2014), https://doi.org/10.1063/1.4901836.

[7] M. Terrones, A. Voshell, M.M. Rana, Review of Optical Properties of Two-Dimensional Transition Metal Dichalcogenides, 2018, p. 21, https://doi.org/10.1117/12.2323132.

[8] M. Shanmugam, T. Bansal, C.A. Durcan, B. Yu, Schottky-barrier solar cell based on layered semiconductor tungsten disulfide nanofilm, Appl. Phys. Lett. 101 (2012), 263902, https://doi.org/10.1063/1.4773525.

[9] A.K. Patel, B.P. Pandey, Performance analysis of WS2 TMD material as an absorber layer used in solar cell, Int. Conf. Electr. Electron. Eng. ICE3 (2020) 382–384, https://doi.org/10.1109/ICE348803.2020.9122856, 2020.

[10] N. Sakhuja, R.K. Jha, N. Bhat, Tungsten disulphide nanosheets for high-performance chemiresistive ammonia gas sensor, IEEE Sensor. J. 19 (2019) 11767–11774, https://doi.org/10.1109/JSEN.2019.2936978.

[11] D.J. Late, R.v. Kanawade, P.K. Kannan, C.S. Rout, Atomically thin WS2 nanosheets based gas sensor, Sens. Lett. 14 (2016) 1249–1254, https://doi.org/10.1166/SL.2016.3764.

[12] S. Sharma, S. Bhagat, J. Singh, R.C. Singh, S. Sharma, Excitation-dependent photoluminescence from WS2 nanostructures synthesized via top-down approach, J. Mater. Sci. 52 (2017) 11326–11336, https://doi.org/10.1007/S10853-017-1303-3/FIGURES/11.

[13] H.G. Ji, P. Solís-Fernández, U. Erkllç, H. Ago, Stacking orientation-dependent photoluminescence pathways in artificially stacked bilayer WS2Nanosheets grown by chemical vapor deposition: implications for spintronics and valleytronics, ACS Appl. Nano Mater. 4 (2021) 3717–3724, https://doi.org/10.1021/ACSANM.1C00192.

[14] R.K. Jha, P.K. Guha, Liquid exfoliated pristine WS2 nanosheets for ultrasensitive and highly stable chemiresistive humidity sensors, Nanotechnology 27 (2016), 475503, https://doi.org/10.1088/0957-4484/27/47/475503.

[15] G. Chen, H. Li, H. Guan, H. Lu, J. Dong, J. Yu, J. Zhang, M. Jiang, W. Zhu, W. Qiu, X. Wang, Y. Zhong, Y. Luo, Z. Chen, Z. Zhang, Highly sensitive all-optical control of light in WS_2 coated microfiber knot resonator, Opt Express 26 (Issue 21) (2018) 27650–27658, https://doi.org/10.1364/OE.26.027650, 27650–27658.

[16] H. Long, L. Tao, C.Y. Tang, B. Zhou, Y. Zhao, L. Zeng, S.F. Yu, S.P. Lau, Y. Chai, Y. H. Tsang, Tuning nonlinear optical absorption properties of WS2 nanosheets, Nanoscale 7 (2015) 17771–17777, https://doi.org/10.1039/C5NR04389A.

[17] Y. Shi, H. Li, L.J. Li, Recent advances in controlled synthesis of two-dimensional transition metal dichalcogenides via vapour deposition techniques, Chem. Soc. Rev. 44 (2015) 2744–2756, https://doi.org/10.1039/C4CS00256C.

[18] L. Zeng, L. Tao, C. Tang, B. Zhou, H. Long, Y. Chai, S.P. Lau, Y.H. Tsang, High-responsivity UV-Vis photodetector based on transferable WS2 film deposited by Magnetron sputtering, Sci. Rep. 6 (2016) 1–8, https://doi.org/10.1038/srep20343, 2016 6:1.

[19] T.A.J. Loh, D.H.C. Chua, A.T.S. Wee, One-step synthesis of few-layer WS2 by pulsed laser deposition, Sci. Rep. 5 (1) (2015) 1–9, https://doi.org/10.1038/srep18116, 2015, 5.

[20] C.M. Orofeo, S. Suzuki, Y. Sekine, H. Hibino, Scalable synthesis of layer-controlled WS2 and MoS2 sheets by sulfurization of thin metal films, Appl. Phys. Lett. 105 (2014), 083112, https://doi.org/10.1063/1.4893978.

[21] Y. Lee, J.W. Jung, J.S. Lee, Highly electroconductive and uniform WS2 film growth by sulfurization of W film using diethyl sulfide, Mater. Chem. Front. 5 (2021) 3692–3698, https://doi.org/10.1039/D1QM00173F.

[22] R. Lv, J.A. Robinson, R.E. Schaak, D. Sun, Y. Sun, T.E. Mallouk, M. Terrones, Transition metal dichalcogenides and beyond: synthesis, properties, and applications of single- and few-layer nanosheets, Acc. Chem. Res. 48 (2014) 56–64, https://doi.org/10.1021/AR5002846.

[23] B. Adilbekova, Y. Lin, E. Yengel, H. Faber, G. Harrison, Y. Firdaus, A. El-Labban, D. H. Anjum, V. Tung, T.D. Anthopoulos, Liquid phase exfoliation of MoS2 and WS2 in aqueous ammonia and their application in highly efficient organic solar cells, J. Mater. Chem. C 8 (2020) 5259–5264, https://doi.org/10.1039/D0TC00659A.

[24] B.H. Kim, H. Yoon, S.H. Kwon, D.W. Kim, Y.J. Yoon, Direct WS2 photodetector fabrication on a flexible substrate, Vacuum 184 (2021), https://doi.org/10.1016/J.VACUUM.2020.109950.

[25] B.H. Kim, H.H. Gu, Y.J. Yoon, Large-area and low-temperature synthesis of few-layered WS2 films for photodetectors, 2D Mater. 5 (2018), 045030, https://doi.org/10.1088/2053-1583/AADEF8.

[26] J. Li, J. Han, H. Li, X. Fan, K. Huang, Large-area, flexible broadband photodetector based on WS2 nanosheets films, Mater. Sci. Semicond. Process. 107 (2020), 104804, https://doi.org/10.1016/J.MSSP.2019.104804.

[27] J. Xu, X. Cheng, T. Liu, Y. Yu, L. Song, Y. You, T. Wang, J. Zhang, Oxygen-incorporated and layer-by-layer stacked WS2 nanosheets for broadband, self-driven and fast-response photodetection, Nanoscale 11 (2019) 6810–6816, https://doi.org/10.1039/C8NR10350J.

[28] X. Ren, B. Wang, Z. Huang, H. Qiao, C. Duan, Y. Zhou, J. Zhong, Z. Wang, X. Qi, Flexible self-powered photoelectrochemical-type photodetector based on 2D WS2-graphene heterojunction, FlatChem 25 (2021), 100215, https://doi.org/10.1016/J.FLATC.2020.100215.

[29] X. Zhang, H. Xu, J. Wang, X. Ye, W. Lei, M. Xue, H. Tang, C. Li, Synthesis of ultrathin WS2 nanosheets and their tribological properties as lubricant additives, Nanoscale Res. Lett. 11 (2016), https://doi.org/10.1186/S11671-016-1659-3.

[30] M. Tayebi, Z. Masoumi, B.K. Lee, Ultrasonically prepared photocatalyst of W/WO3 nanoplates with WS2 nanosheets as 2D material for improving photoelectrochemical water splitting, Ultrason. Sonochem. 70 (2021), 105339, https://doi.org/10.1016/J.ULTSONCH.2020.105339.

[31] I. Paradisanos, N. Pliatsikas, P. Patsalas, C. Fotakis, E. Kymakis, G. Kioseoglou, E. Stratakis, Spatial Non-uniformity in Exfoliated WS 2 Single Layers, (n.d.). Nanoscale 8 (2016), 16197-16203, doi.org/10.1039/C6NR03597C.

[32] S. Salehi, A. Saffarzadeh, Atomic defect states in monolayers of MoS2 and WS2, Surf. Sci. 651 (2016) 215–221, https://doi.org/10.1016/J.SUSC.2016.05.003.

[33] G. Pradhan, A.K. Sharma, Linear and nonlinear optical response of sulfur-deficient nanocrystallite WS2 thin films, J. Mater. Sci. 54 (2019) 14809–14824, https://doi.org/10.1007/S10853-019-03986-8/FIGURES/13.

[34] S. Baroni, S. de Gironcoli, A. Dal Corso, P. Giannozzi, Phonons and related crystal properties from density-functional perturbation theory, Rev. Mod. Phys. 73 (2001) 515, https://doi.org/10.1103/RevModPhys.73.515.

[35] L. Zhang, A. Zunger, Evolution of electronic structure as a function of layer thickness in group-VIB transition metal dichalcogenides: emergence of localization prototypes, Nano Lett. 15 (2015) 949–957, https://doi.org/10.1021/NL503717P/SUPPL_FILE/NL503717P_SI_001.PDF.

[36] H.R. Gutiérrez, N. Perea-López, A.L. Elías, A. Berkdemir, B. Wang, R. Lv, F. López-Urías, V.H. Crespi, H. Terrones, M. Terrones, Extraordinary room-temperature photoluminescence in triangular WS 2 monolayers, Nano Lett. 13 (2013) 3447–3454, https://doi.org/10.1021/NL3026357/SUPPL_FILE/NL3026357_SI_001.PDF.

[37] K.K. Kam, B.A. Parkinson, Detailed photocurrent spectroscopy of the semiconducting group VIB transition metal dichalcogenides, J. Phys. Chem. 86 (2002) 463–467, https://doi.org/10.1021/J100393A010.

[38] N. Perea-Lõpez, A.L. Elías, A. Berkdemir, A. Castro-Beltran, H.R. Gutiérrez, S. Feng, R. Lv, T. Hayashi, F. Lõpez-Urías, S. Ghosh, B. Muchharla, S. Talapatra, H. Terrones, M. Terrones, Photosensor device based on few-layered WS2 films, Adv. Funct. Mater. 23 (2013) 5511–5517, https://doi.org/10.1002/ADFM.201300760.

[39] A. Aldalbahi, T. Ahamad, S.M. Alshehri, Z.B. Wang, P.X. Feng, Three-dimensional architectures composed of two-dimensional atomic layer molybdenum disulphide for solar cell and self-powered photodetectors with improved performance, Https://Doi.Org/10.1177/01445987211036828, https://doi.org/10.1177/01445987211036828, 2021.

[40] J.D. Yao, Z.Q. Zheng, J.M. Shao, G.W. Yang, Stable, highly-responsive and broadband photodetection based on large-area multilayered WS2 films grown by pulsed-laser deposition, Nanoscale 7 (2015) 14974–14981, https://doi.org/10.1039/C5NR03361F.

[41] C. Lan, Z. Zhou, Z. Zhou, C. Li, L. Shu, L. Shen, D. Li, R. Dong, S. Yip, J.C. Ho, Wafer-scale synthesis of monolayer WS 2 for high-performance flexible photodetectors by enhanced chemical vapor deposition, Nano Res. 11 (2018) 3371–3384, https://doi.org/10.1007/s12274-017-1941-4.